

Bucknell University

Bucknell Digital Commons

Faculty Journal Articles

Faculty Scholarship

11-28-2016

Solid Stress and Elastic Energy as Measures of Tumour Mechanopathology

Hadi T. Nia

Massachusetts General Hospital

Hao Liu

Massachusetts General Hospital

Giorgio Seano

Massachusetts General Hospital

Meenal Datta

Tufts University

Dennis Jones

Massachusetts General Hospital

See next page for additional authors

Follow this and additional works at: https://digitalcommons.bucknell.edu/fac_journ

Recommended Citation

Nia, Hadi T.; Liu, Hao; Seano, Giorgio; Datta, Meenal; Jones, Dennis; Rahbari, Nuh; Incio, Joao; Chauhan, Vikash P.; Jung, Keehoon; Martin, John D.; Askoxylakis, Vasileios; Padera, Timothy P.; Fukumura, Dai; Boucher, Yves; Hornicek, Francis J.; Grodzinsky, Alan J.; Baish, James W.; Munn, Lance L.; and Jain, Rakesh K.. "Solid Stress and Elastic Energy as Measures of Tumour Mechanopathology." *Nature Biomedical Engineering* (2016) : 0004.

This Article is brought to you for free and open access by the Faculty Scholarship at Bucknell Digital Commons. It has been accepted for inclusion in Faculty Journal Articles by an authorized administrator of Bucknell Digital Commons. For more information, please contact dcadmin@bucknell.edu.

Authors

Hadi T. Nia, Hao Liu, Giorgio Seano, Meenal Datta, Dennis Jones, Nuh Rahbari, Joao Incio, Vikash P. Chauhan, Keehoon Jung, John D. Martin, Vasileios Askoxylakis, Timothy P. Padera, Dai Fukumura, Yves Boucher, Francis J. Hornicek, Alan J. Grodzinsky, James W. Baish, Lance L. Munn, and Rakesh K. Jain

Solid stress and elastic energy as measures of tumour mechanopathology

Hadi T. Nia¹, Hao Liu^{1,2}, Giorgio Seano¹, Meenal Datta^{1,3}, Dennis Jones¹, Nuh Rahbari¹, Joao Incio^{1,4}, Vikash P. Chauhan¹, Keehoon Jung¹, John D. Martin¹, Vasileios Askoxylakis¹, Timothy P. Padera¹, Dai Fukumura¹, Yves Boucher¹, Francis J. Hornicek⁵, Alan J. Grodzinsky⁶, James W. Baish⁷, Lance L. Munn¹ and Rakesh K. Jain^{1*}

Solid stress and tissue stiffness affect tumour growth, invasion, metastasis and treatment. Unlike stiffness, which can be precisely mapped in tumours, the measurement of solid stresses is challenging. Here, we show that 2D spatial maps of the solid stress and the resulting elastic energy in excised or *in situ* tumours with arbitrary shapes and a wide range of sizes can be obtained via three distinct and quantitative techniques that rely on the measurement of tissue displacement after disruption of the confining structures. Application of these methods in models of primary tumours and metastasis revealed that (i) solid stress depends on both cancer cells and their microenvironments, (ii) solid stress increases with tumour size and (iii) mechanical confinement by the surrounding tissue substantially contributes to intratumoral solid stress. Further study of the genesis and consequences of solid stress, facilitated by the engineering principles presented here, may lead to new discoveries and therapies.

Increased tissue stiffness is a widely accepted and actively studied biomechanical property of fibrotic tumours and has been linked to several hallmarks of cancer, including growth, metabolism, invasion and metastasis^{1–7}. However, the abnormal mechanics of tumours are not limited to tissue stiffening. We recently demonstrated that solid stress represents a new mechanopathology that is consistently elevated in mouse and human tumours^{8,9}. Solid stress is distinct from interstitial fluid pressure, as the former is contained in—and transmitted by—solid and elastic elements of the extracellular matrix and cells rather than fluids¹⁰. Therefore, tumours are not only more rigid than many normal tissues, but cancer cells also produce and are exposed to these physical forces. Composed of a combination of tension and compression, these forces are significant in tumours, but negligible in most normal tissues.

Early evidence for the existence of solid stress in tumours came from the discovery that blood and lymphatic vessels are mechanically compressed^{11–13}. This can contribute to hypoxia^{9,14}, promote tumour progression and decrease the efficacy of chemo-, radio- and immunotherapies¹⁵. In addition to these physiological consequences, forces can directly affect tumour biology: the exogenous application of solid stress *in vivo* can mechanically stimulate tumorigenic pathways, increasing β -catenin signalling in colon epithelia¹⁶, and the controlled application of compressive forces *in vitro* affects the growth⁸ of cancer cells and promotes their collective migration¹⁷. Strategies designed to reduce solid stress and decompress blood vessels by reducing levels of collagen and hyaluronic acid^{14,18,19} have led to therapeutic approaches for enhancing the efficiency of conventional anticancer treatments and are currently being tested in clinical trials^{20,21}.

Despite the important implications of solid stress and the immense potential for finding new mechanically activated pathways and targets, there are currently no high-resolution methods for quantifying solid stress in experimental or human tumours. Unlike stiffness, which can be measured using widely available multiscale techniques, measuring solid stress in biological tissues has proved challenging. Previous studies in our laboratory^{8,9}, based on previous observations^{22,23} that arterial wall tissue relaxes if the contained forces are surgically released, demonstrated the presence of residual tissue stresses in tumours. However, this approach is based on a partial cut through a spherical model of the tumour, which makes the precise release of solid stress and the measurement of the ensuing deformation challenging. This method is also limited to bulk estimation of solid stress and is not applicable *in situ*. The optical-depth limitations of alternative imaging-based methods, such as fluorescent oil microdroplet injection²⁴ and single-molecule fluorescent force sensors²⁵, restrict their use to cellular- and subcellular-scale force detection.

We have developed experimental and mathematical frameworks to provide 2D mapping of solid stress in tumours (planar-cut method), sensitive estimations of the solid stress in small tumours with small magnitudes of solid stress, as is the case for metastatic lesions (slicing method), and *in situ* quantification of solid stress in tumours, which retains the effects of the normal surrounding tissues (needle-biopsy method). All three methods are based on the concept of releasing the solid stress in a controlled way with a defined geometry and then quantifying the stress-induced deformation via high-resolution ultrasonography or optical microscopy. Given the specific topography of the stress relaxation and the geometric

¹Edwin L. Steele Laboratories, Department of Radiation Oncology, Massachusetts General Hospital, Harvard Medical School, Boston, Massachusetts 02114, USA. ²Leder Human Biology and Translational Medicine, Biology and Biomedical Sciences, Harvard Medical School, Boston, Massachusetts 02115, USA.

³Department of Chemical and Biological Engineering, Tufts University, Medford, Massachusetts 02155, USA. ⁴Department of Internal Medicine, Hospital S. Joao, I3S, Institute for Innovation and Research in Health, and Faculty of Medicine, Porto University, 4200-319 Porto, Portugal. ⁵Orthopedic Oncology Service, Center for Sarcoma and Connective Tissue Oncology, Massachusetts General Hospital, Harvard Medical School, Boston, Massachusetts 02114, USA. ⁶Center for Biomedical Engineering, Departments of Mechanical, Electrical and Biological Engineering, Massachusetts Institute of Technology, Cambridge, Massachusetts 02139, USA. ⁷Department of Biomedical Engineering, Bucknell University, Lewisburg, Pennsylvania 17837, USA. *e-mail: jain@steele.mgh.harvard.edu

and material properties of the tumour, solid stress and discharged elastic energy are estimated using mathematical modelling. Applying these methods to multiple mouse cancer models in primary and metastatic settings has led to the following findings: (i) solid stress and elastic energy may differ between primary and metastatic settings, as they depend on both cancer-cell type and their microenvironment; (ii) tumours with higher elastic energy are not necessarily stiffer, and the stiffer tumours do not necessarily have higher elastic energy; (iii) solid stress increases with tumour size; and (iv) the normal tissue surrounding a tumour substantially contributes to intratumoral solid stress.

2D mapping of the solid stress

To produce a 2D map of the solid stress, we made a clean cut through freshly excised tumours embedded in 2% agarose (Fig. 1a). The planar cut removes the mechanical confinement at the cut surface and allows this face of the tumour to deform accordingly, as previously predicted by our mathematical model⁹. The deformation is a measure of the stored elastic energy in the tissue caused by solid stress (Fig. 1b). The deformation in the z direction, $u_z(x, y)$, imaged over the x - y cross-section of the tumour, is an indicator of the magnitude and direction of the solid stress in the z direction at the incision plane: regions with positive deformation (bulged) were under compression and regions with negative deformation (depressed) were under tension (Fig. 1a,b). For tissues with negligible solid stress, such as normal kidney and liver tissues, deformation was negligible and uniform across the incision surface (Fig. 1c). The deformation is spatially mapped in 3D via high-resolution ultrasound (resolution of 30 μm). By developing a mathematical model (a 3D finite-element model; Fig. 1b), the 2D map of deformation u_z is converted to the strain tensor $\varepsilon_{ij} = 1/2(\partial u_i / \partial x_j + \partial u_j / \partial x_i)$, from which the stress tensor σ_{ij} is estimated on the basis of Hooke's law²⁶, written in index notation as

$$\sigma_{ij} = \frac{E}{(1+\nu)} \left(\varepsilon_{ij} + \frac{\nu}{(1+2\nu)} \varepsilon_{kk} \delta_{ij} \right) \quad (1)$$

where E is Young's modulus (stiffness), ν is Poisson's ratio of the tissue (assuming linear isotropicity) and δ_{ij} is the Kronecker delta. We used the average Young's modulus of the tumour, measured via an unconfined compression test at the macroscale or via atomic force microscopy measurements at multiple indentation sites. However, the finite-element model is capable of incorporating the previously reported 3D stiffness heterogeneities of the tumour^{27,28}. Since the cut fully releases the stress component σ_{zz} at the cut plane, we report only this stress component at the cut surface throughout this study. The other stress components, such as the stresses in the x - y plane, are also affected and accounted for in the 3D model. However, since the planar-cut method does not fully release these stresses, we do not report them in this study.

Similar to a spring that is compressed (Fig. 1b), the solid-stress field does mechanical work as it accumulates in the tumour; this work is stored as elastic potential energy during tumour growth. The elastic energy density, W , released by the incision is calculated from the following equation²⁶ for a tumour half with volume V :

$$W = \frac{1}{2V} \int_V \sigma_{ij} \varepsilon_{ij} dV \quad (2)$$

Although W is averaged over the volume of the tumour hemisphere, it is not equivalent to the total elastic energy of the tumour. The elastic energy W is only the energy that is released from the relaxation of the solid stress at the desired cut plane; for the locations far from the cut plane, the elastic energy and solid stress are not fully released. To enable an estimation of the total elastic energy in a tumour, it would need to be cut into infinitesimally

small pieces to release all of the solid stress and elastic energy. The elastic energy is not independent of solid stress; however, it describes the tensor-based stress field more sensitively and in the form of a single scalar quantity. Furthermore, elastic energy rigorously differentiates between the forces emanating from the solid versus fluid phases¹ of the tumour on the basis of the following considerations: (i) the interstitial fluid is incompressible, so the fluid pressure cannot do work on the fluid phase of the tumour; and (ii) the solid phase is porous and fluid can flow through it, so the fluid pressure cannot do work on the solid phase of the tumour in quasi-equilibrium events, such as tumour growth.

Using the planar-cut method, we mapped solid stress for three mouse models of orthotopically implanted primary tumours: breast (adenocarcinoma, MMTV-M3C), pancreatic (pancreatic ductal adenocarcinoma (PDAC), AK4.4) and brain (glioblastoma, U87) (Fig. 1d). For each model, a representative ultrasound image shows the stress-induced deformation quantified with respect to the cut plane (yellow dashed lines). The 2D deformations obtained via quantification of δ_z based on the reference incision plane from ultrasound images, the 2D map of the solid stress σ_{zz} , estimated from the finite-element model, and the profile of σ_{zz} across the bisecting dashed lines are shown in the lower panels. The 2D maps of σ_{zz} in the breast and pancreatic tumours show a common pattern of compressive stresses in the central regions, and tensile stresses with higher magnitude in narrow peripheral regions. However, in the U87 model of glioblastoma, the tumour experiences compressive stresses over annular regions close to the periphery, rather than in the centre of the tumour. The maximum value of the solid stress varies from 0.21 kPa (1.56 mmHg) in brain tumours to 7 kPa (52.5 mmHg) in pancreatic tumours (which are highly desmoplastic). The planar-cut method is capable of estimating a large dynamic range of solid stresses in addition to the variation in the pattern of the compressive and tensile stresses stored in different tumour types. We also demonstrated the planar-cut method on human chondrosarcoma tumours, for which the 2D deformation maps are shown in Supplementary Fig. 1.

We hypothesized that structural elements such as collagen fibres are critical to transmitting solid stress^{9,14}. To test this hypothesis, we enzymatically depleted collagen in the MMTV-M3C model of breast cancer using a collagenase treatment *ex vivo*. We showed that the average magnitude of the solid stress $\langle |\sigma_{zz}| \rangle$ was reduced by a factor of more than two, whereas the elastic energy density W was reduced by a factor of more than six (Fig. 1e).

The microenvironment influences solid stress

Little is known about how biomechanical abnormalities vary between primary and metastatic lesions or how these differences affect tumour biology. To address this, we used the planar-cut method to estimate and compare the solid stress, elastic energy and mechanical stiffness in size-matched tumours formed from the same cell lines, and in primary versus metastatic sites.

We found that primary PDAC AK4.4 tumours had much higher levels of solid stress than PDAC liver metastases (Fig. 2a,b), despite the fact that both tumours were formed by the same cell line and were approximately size matched. Since these two tumours have similar elastic moduli (Fig. 2e), the higher deformation after incision results in higher stress values (Fig. 2f) and higher elastic energies (Fig. 2g) in primary sites than in liver metastases. This comparison shows that AK4.4 tumours growing in the pancreas generate a higher solid stress and store more elastic energy than AK4.4 liver metastases. Interestingly, this trend is reversed in colorectal carcinomas (Fig. 2c,d): the primary colorectal tumours have lower levels of solid stress and elastic energy than colorectal cancer liver metastases, despite having similar elastic moduli. Our data show that the growth in the liver microenvironment does not always result in lower stored elastic energy. An interesting comparison can also be made between metastases of different cancer cells in the same host organ (in this

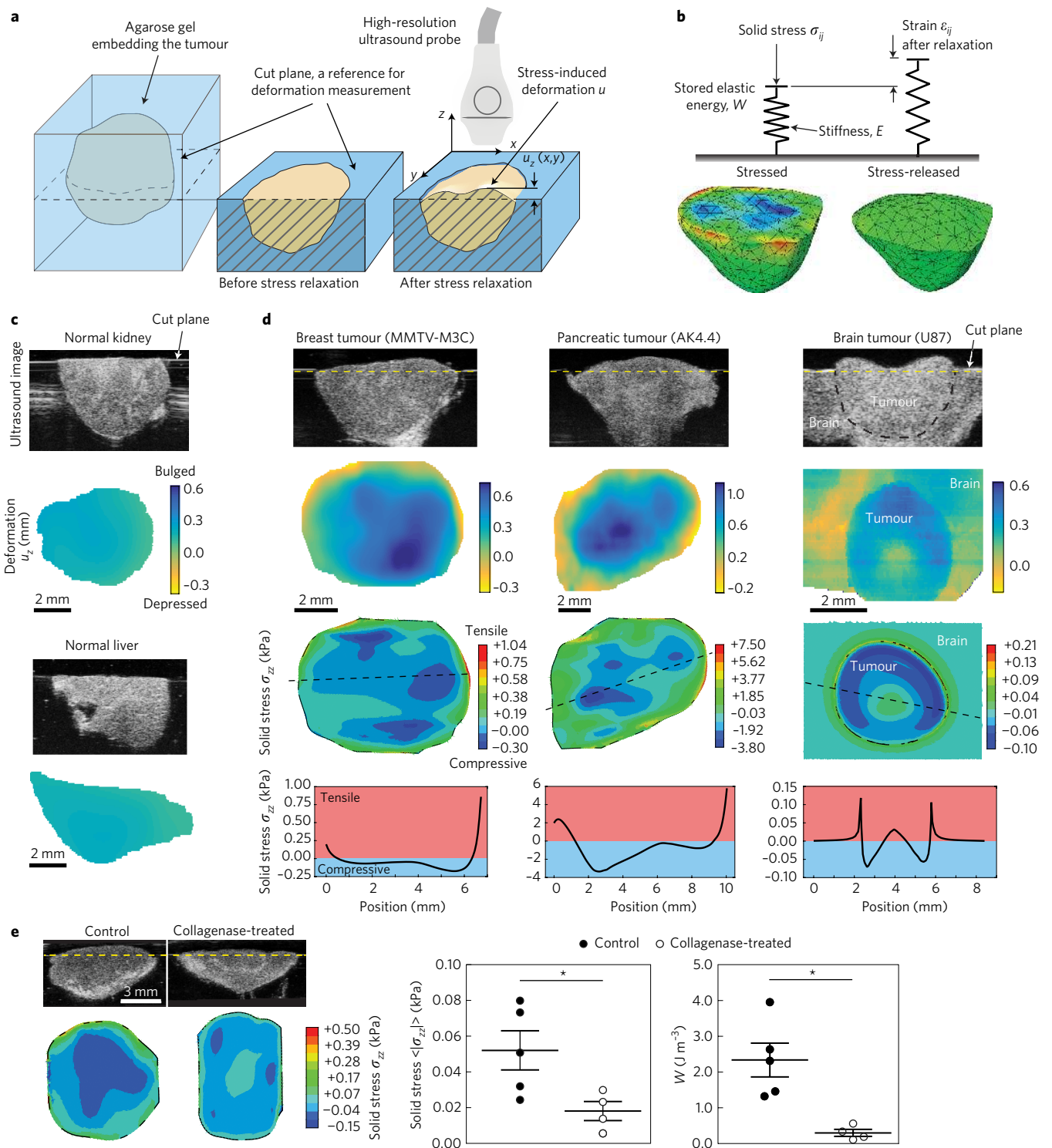


Figure 1 | 2D maps of solid stress in tumours. **a**, The fresh tumour was embedded in 2% agarose (liquid at 40 °C), and then gellated in ice water. The tumour-agarose construct was incised at the plane of interest to release solid stress. The release of solid stress resulted in a deformation field $\delta_z(x,y)$ with respect to the agarose reference plane; δ_z and the tumour geometry were quantified via high-resolution ultrasound (resolution of 20 μm). **b**, Using a finite-element model, σ_{zz} , the mechanical stress in the z direction, and W , the elastic energy stored by solid stress, were estimated from the deformation δ_z and Young’s modulus of the tissue on the basis of Hooke’s law. **c**, The stress-induced deformation δ_z was uniform and negligible in stress-free normal tissues (for example, kidney (top) and liver (bottom)). **d**, Representative ultrasound images showing the stress-induced deformation and agarose reference line (yellow dashed line), 2D deformation fields δ_z , 2D stress fields σ_{zz} , and representative stress profiles across the tumour diameter, all for mouse models of breast tumour (MMTV-M3C), pancreatic ductal adenocarcinoma tumour (AK4.4) and brain tumour (glioblastoma, U87). **e**, Enzymatic depletion of collagen in a (MMTV-M3C) breast tumour resulted in notable reduction of solid stress and elastic energy density (control, $n=5$ mice; collagenase-treated, $n=4$ mice; mean \pm standard error of the mean; * $P<0.05$). A representative ultrasound image and a solid-stress map are shown for the control and collagenase-treated tumours.

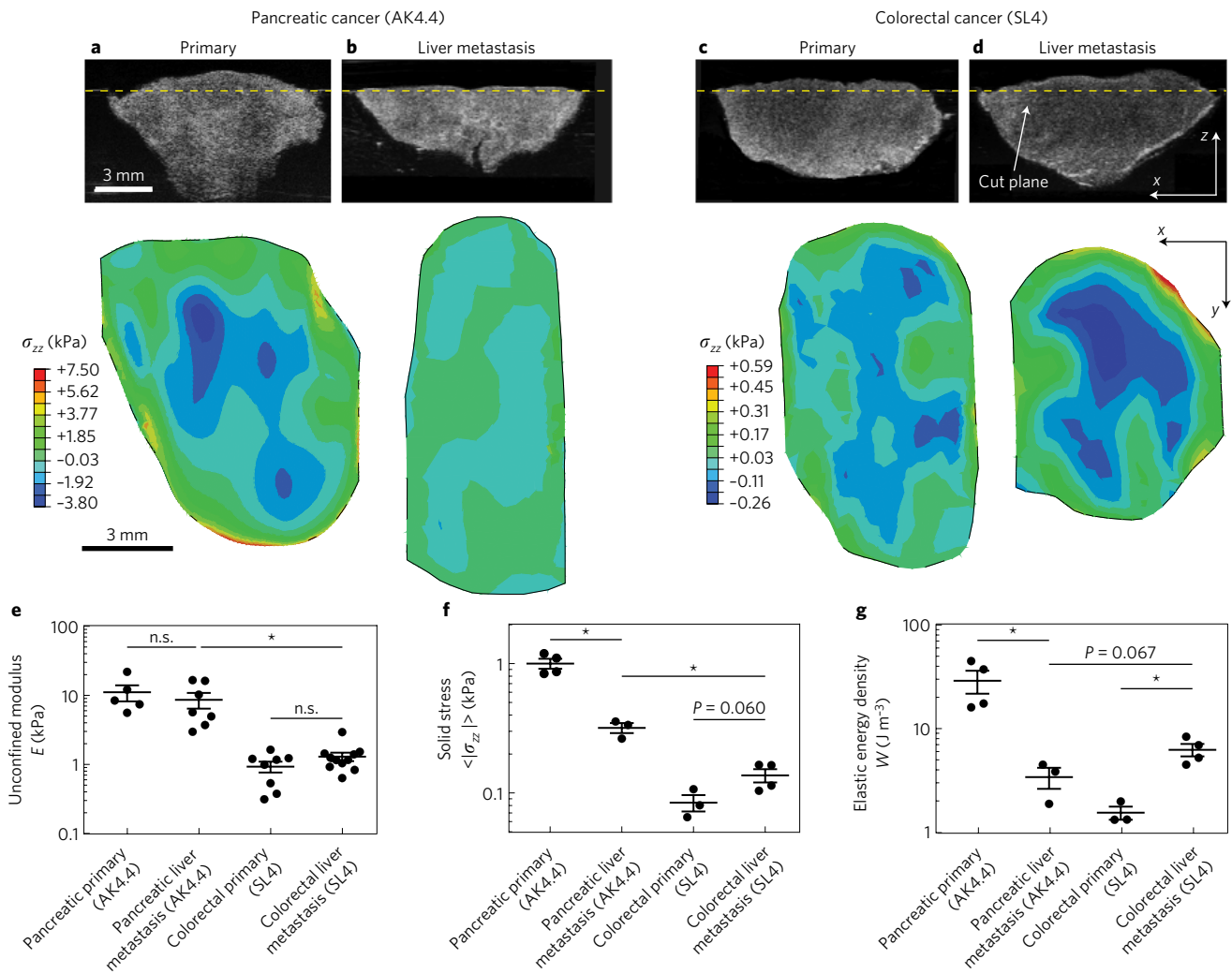


Figure 2 | Solid stress and elastic energy in primary versus metastatic tumours. a–d, Representative ultrasound images and 2D stress maps are shown for size-matched primary pancreatic ductal adenocarcinoma (PDAC, AK4.4; $n = 4$ mice) (a), liver metastasis of PDAC (AK4.4; $n = 3$ mice) (b), primary colorectal carcinoma (SL4; $n = 3$ mice) (c) and liver metastasis of colorectal carcinoma (SL4; $n = 4$ mice) (d). **e–g,** Comparison of Young's modulus (unconfined compression) (e), average solid stress in the z direction, σ_{zz} (f) and elastic energy density (g) in these four tumour models shows that the type of cancer cell is not the only determinant of biomechanical abnormalities: the organ and microenvironment in which the cancer cells reside are equally important in the generation of solid stress and elastic energy in tumours. The data shown are mean \pm the standard error of the mean; n.s., not significant; * $P < 0.05$.

case, the liver). Although the elastic modulus of PDAC liver metastases is fivefold larger than that of the colorectal cancer liver metastases, the elastic energy actually shows the opposite trend. This is due to considerably larger stress-induced deformation in colorectal cancer liver metastasis and to the greater dependence of elastic energy on stress-induced deformation (equation (2)). The solid stress shows a trend that is lower than but similar to the trend of the elastic modulus between the two metastases, as the solid stress follows a linear relationship with the deformation (equation (1)). From the above comparisons we observe that (i) solid stress and elastic energy are mechanical abnormalities that vary between tumours; (ii) solid stress and elastic energy depend on both the cancer-cell type and the microenvironment in which they reside; and (iii) tumours with greater elastic energy are not necessarily stiffer, and stiffer tumours do not necessarily have greater elastic energy.

Tissue slices allow measurements in small tumours

To measure the solid stress and elastic energy in smaller tumours (for example, in micro- and macro-metastases), we developed a more sensitive method—also based on releasing elastic energy—by slicing the tissue into thin slices (Fig. 3a). Again, the freshly

excised tumour is embedded in 2% agarose, which is then sliced by a vibratome with a desired thickness in the range 100–500 μm . The tumour slice, originally flat, undergoes expansion and contraction in the area of the slice when the in-plane stresses and elastic energy are released (Supplementary Fig. 2), as demonstrated in models of breast tumours (MMTV-M3C), pancreatic tumours (PDAC, AK4.4) and lymph-node metastasis of breast cancer (4T1) (Fig. 3b–d). Inhomogeneities in the in-plane stresses (shown for the partial release of these stress components in Supplementary Fig. 3) mean that the slice undergoes out-of-plane bending and buckling. This method is more sensitive than the planar-cut method since a thin slice is exposed to more degrees of freedom to deform and reacts to even small levels of solid stress. The deformed slices are then imaged in 3D using high-resolution ultrasound (used here for AK4.4 and MMTV-M3C tumours) or optical frequency domain imaging (OFDI; used here for lymph node metastasis)²⁹ after stress relaxation. The compressive and tensile stresses (as mapped in Fig. 1d) are released in different ways: the compressive forces are released by the slice volume expanding (which results in lateral bending and buckling) and the tensile forces are released by the periphery of the tumours pulling inwards. Thus, the complex geometry

formed from an originally flat disc-shaped slice is the result of non-uniformity and coexisting residual tension–compression in-plane stresses released in the slice. We used this method on normal kidney and lymph node micro-metastases, and observed negligible deformation after slicing (Fig. 3e,f), consistent with the results of the planar-cut method (Fig. 1c).

The release of elastic energy via slicing results in the expansion of the surface area of the slice. The overall area expansion after slicing represents the area strain, a quantitative index for in-plane solid stresses and the stored elastic energy in the slice. We defined the area-expansion ratio as follows:

$$I_{ER} = \frac{A_{\text{tumour}} - A_{\text{blank}}}{A_{\text{blank}}} \quad (3)$$

where A_{tumour} is the surface area of the tumour slice after the elastic energy is released and obtained from the 3D image of the slice, and A_{blank} is the reference area of the tumour slice before slicing, obtained from the empty space left in the agarose gel (Fig. 3h,i). The expansion ratio has been quantified as $30.7 \pm 5.8\%$ for the breast tumour, $34.0 \pm 4.9\%$ for the PDAC and $17.2 \pm 1.2\%$ for the lymph node with breast cancer macro-metastasis, which are considerably higher than the control tissues: $7.0 \pm 1.9\%$ for the kidney and $5.0 \pm 1.2\%$ for the lymph node with micro-metastasis (Fig. 3j and Supplementary Fig. 4). Note that with this method the tumour undergoes consecutive cuts before the desired tumour slice is obtained. In doing so, the out-of-plane stresses (σ_{zz}) are fully released, similar to the planar-cut method. In addition, the in-plane stresses (σ_{xx} and σ_{yy}) are also partially released, as shown in the example in Supplementary Fig. 3. For the representative case of the MMTV-M3C model of breast cancer, we showed that the slicing method releases the majority of the in-plane stresses compared with the relaxation of in-plane stresses that occurs before the slicing. The average area strain obtained via the slicing method in the MMTV-M3C model is $I_{ER} = 30.7\%$, which results in $\langle \sigma_{\text{in-plane}} \rangle = 0.27 \text{ kPa}$ ($E = 0.87 \text{ kPa}$). However, the average σ_{xx} and σ_{yy} released by the cuts prior to the desired slicing are 0.069 kPa and 0.078 kPa (Supplementary Fig. 3), respectively, no larger than one-third of $\langle \sigma_{\text{in-plane}} \rangle$, which shows that the majority of the in-plane stresses are relaxed when using the slice method and are thus reported as area strain I_{ER} (equation (3)).

Evolution of solid stress during tumour growth

Investigating the accumulation of solid stress as a function of tumour growth provides invaluable information regarding both the genesis and the implications of solid stress. We used the slice method to measure I_{ER} (equation (3)) induced by the relaxation of solid stress in MMTV-M3C breast tumours, for tumours ranging in size from 2 to 7 mm in diameter (Fig. 4a). The elastic modulus was also measured via atomic force microscopy (AFM)-based indentation for a similar range of tumour sizes. The expansion ratio (equation (3)) induced by the relaxation of in-plane stresses in the slice increased considerably with increasing tumour diameter (Fig. 4a,b). Tumours with small diameters (2–3 mm) did not show a notable increase in area after slicing, whereas the larger tumours showed an area expansion of up to 30–40%. Notably, the AFM-based indentation modulus did not show any substantial trend with tumour diameter (Fig. 4c). This confirms that solid stress and elastic energy can be considered as mechanical abnormalities distinct from stiffness.

The type I collagen (collagen I) network becomes more organized and more localized at the periphery with increasing tumour size in the MMTV-M3C breast tumour model, consistent with the increase in solid stress. As shown via immunofluorescence analysis, the type I collagen network is uniformly and randomly distributed in smaller tumours (diameter ~2 mm; Fig. 4d) and becomes more localized and organized at the periphery in larger tumours (diameter ~7 mm). To quantitatively describe this collagen I localization

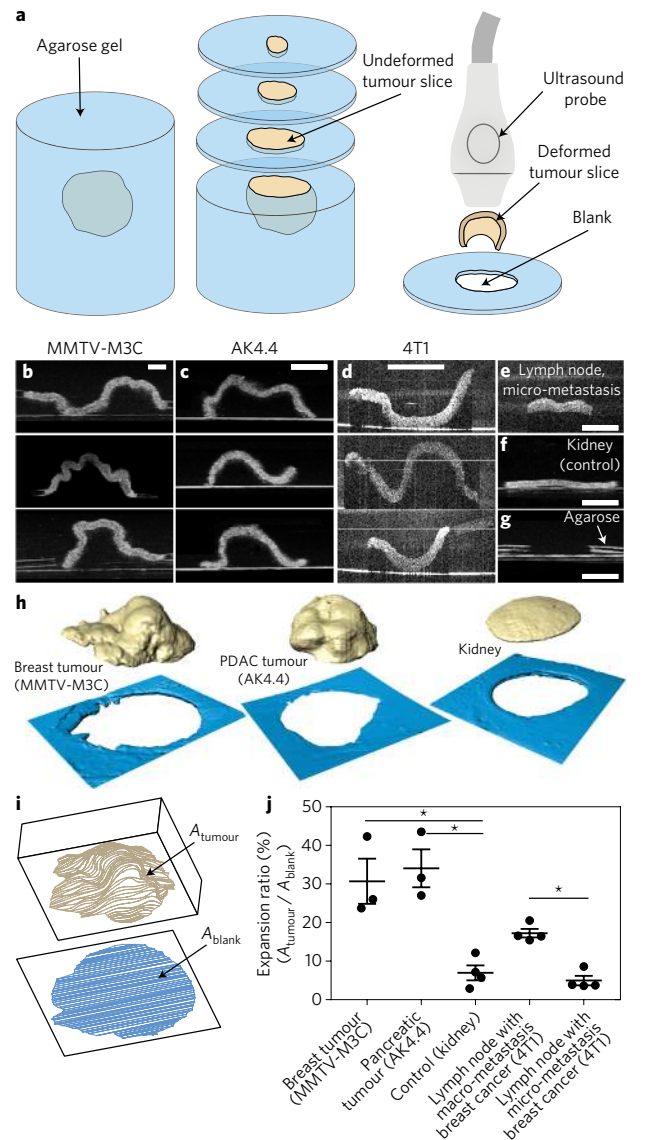


Figure 3 | Creating tumour slices provides a sensitive measure of the solid stress that is applicable to a wide range of specimen sizes.

a, The fresh tumour is embedded in liquid 2% agarose, then sliced with a vibratome and left in phosphate-buffered saline (PBS) at room temperature so that stress-induced deformation occurs in the tumour slice. The deformed slice and the surrounding agarose disc are imaged using high-resolution ultrasound (30 μm resolution) or OFDI (1 μm resolution) for small samples (for example, lymph node). **b–d**, Buckling and deformation of representative slices from breast tumour (MMTV-M3C) (**b**), pancreatic tumour (AK4.4) (**c**) and lymph node with macro-metastasis of breast cancer (4T1) (**d**). **e, f**, Tissues with negligible or low levels of stress, such as lymph node with micro-metastasis (**e**) and kidney (**f**). **g**, The blank space in the agarose disc represents the area of the tumour slice before the stress relaxation. Scale bars, 1 mm. **h**, 3D reconstructions of the slices in breast and pancreatic tumours compared that of with kidney tissue. **i**, The expansion ratio, an index of solid stress and elastic energy, is defined as the ratio of the surface area of the slice after stress relaxation, A_{tumour} , to the area of the blank space in the agarose disc, A_{blank} (equivalent to the area of the slice before stress relaxation). **j**, The expansion ratios in breast ($n=3$ slices) and pancreatic tumours ($n=3$ slices) are substantially higher than the expansion in the kidney slice ($n=3$ slices). The expansion ratio of lymph-node macro-metastasis ($n=4$ slices) is considerably higher than in the micro-metastatic lymph node ($n=4$ slices). The error bars indicate the mean \pm standard error of the mean. PDAC, pancreatic ductal adenocarcinoma. * $P < 0.05$.

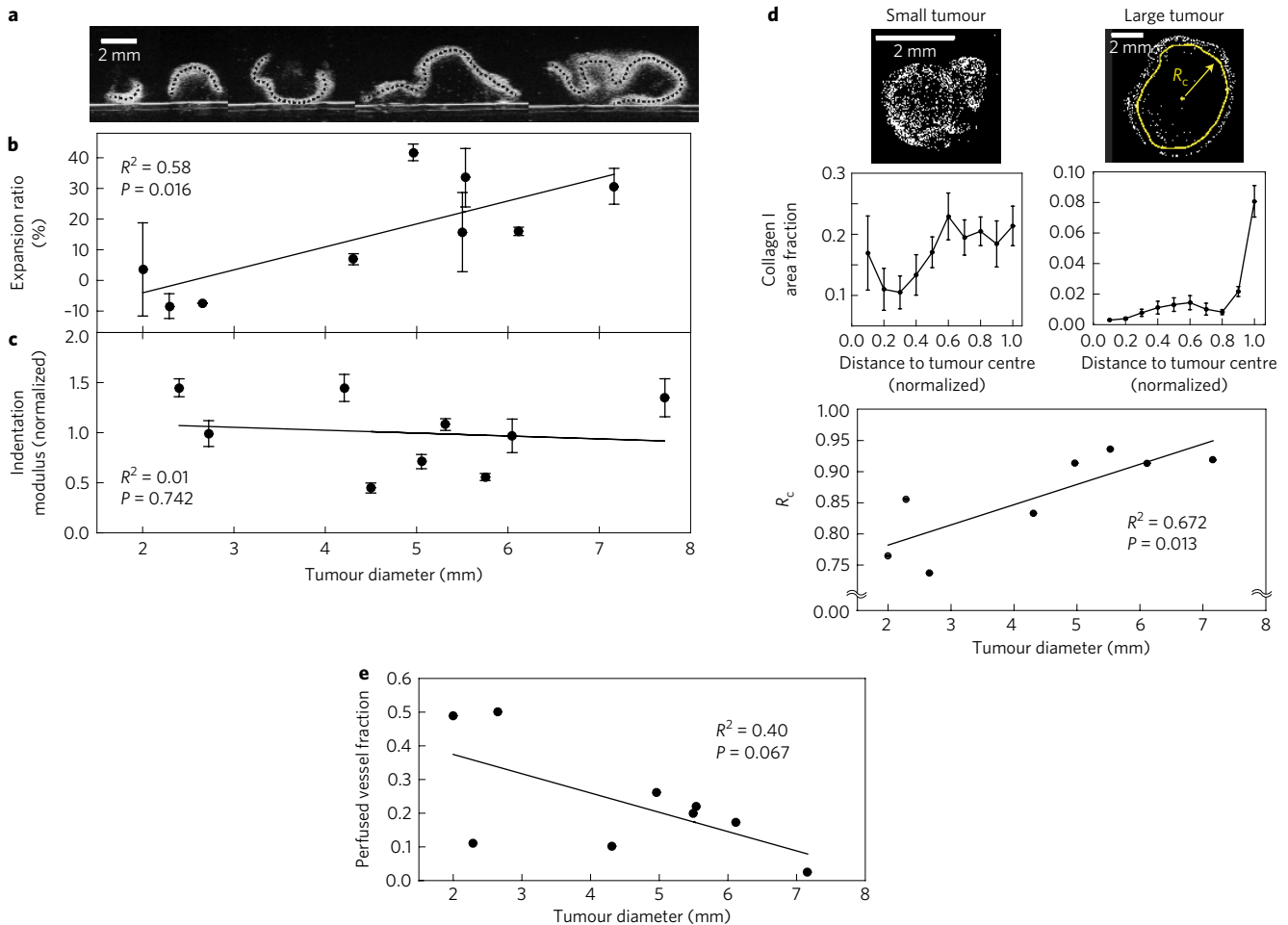


Figure 4 | Evolution of solid stress and stiffness as a function of tumour size. **a**, Solid stress was estimated with the slicing method in breast tumours (MMTV-M3C) with mean diameters ranging from 2 to 7 mm (representative ultrasound images shown). **b**, The expansion ratio—an index of solid stress—increased substantially with increasing tumour size. **c**, The AFM-based indentation modulus of the same tumour model did not vary much with tumour size. **d**, Top: representative immunofluorescence images of collagen I staining (white) of the MMTV-M3C tumours. Middle: the collagen content (assessed by positively stained collagen I area fraction) became localized to the tumour periphery with increasing tumour size. Bottom: the collagen spread radius R_c , defined as the effective normalized radius of an area that contains 50% of the positively stained collagen, increased with tumour diameter. **e**, The fraction of perfused blood vessels shows a decreasing trend with increasing tumour size, consistent with the hypothesis that high solid stress (which increases with tumour size, as shown in **b**) compresses blood vessels¹⁴. The data shown in **b–d** are mean \pm the standard error of the mean. Each data point in **b** represents three slices from each mouse; each tumour diameter is associated with a different mouse. In **c**, each data point represents 10 indentation sites from each mouse. In **d**, ten radial sectors have been quantified for each data point.

effect, we defined a collagen spread radius, R_c , as the radius of an area that contains 50% of the positively stained collagen I. This radius increases substantially with the tumour diameter (Fig. 4d), consistent with a similar increase in area expansion ratio (Fig. 4b). The highly oriented collagen (Supplementary Fig. 5) with increased density at the periphery implies that the periphery of the tumour experiences tensile stresses. This tensile stress in the periphery, consistent with the stress map in Fig. 1d, is hypothesized to originate from the direct contraction of carcinoma-associated fibroblasts^{30,31} or from the resistance to the compressive forces emanating from the volume increase resulting from cell proliferation and extracellular matrix deposition.

Whereas solid stress increased with tumour size, the fraction of perfused vessels showed the opposite trend (Fig. 4e; see also Supplementary Fig. 6 for representative images), consistent with the hypothesis that solid stress can compress blood vessels and decrease tumour perfusion^{9,14,19}. These data also suggest that stiffness, which showed no notable trend with tumour growth for the range of tumour diameters examined in this study, is not

a major contributor to the compression and collapse of intratumoral blood vessels.

The surrounding tissue affects tumour solid stress

So far, we have estimated the solid stress and elastic energy of tumours *ex vivo*, independent of the surrounding normal tissue. Next, via *in situ* estimations of solid stress, we show that the resistance to growth by the surrounding tissue also substantially contributes to the solid stress in the tumour—as previously predicted by our mathematical model^{32,33}. To measure *in situ* solid stresses, we performed a core biopsy of the tumour to create a cylindrical void. We call this the needle-biopsy method. The changes in the diameter of the cylindrical void, measured by ultrasonography, represent a 1D stress profile of the tumour. We first evaluated this method *ex vivo* to release the solid stress in the MMTV-M3C model of breast tumours: the cylindrical void reduced in diameter in the centre and increased in diameter at the periphery of the tumour (Fig. 5b). This deformation profile indicates that there are compressive stresses in the centre and tensile stresses in the periphery

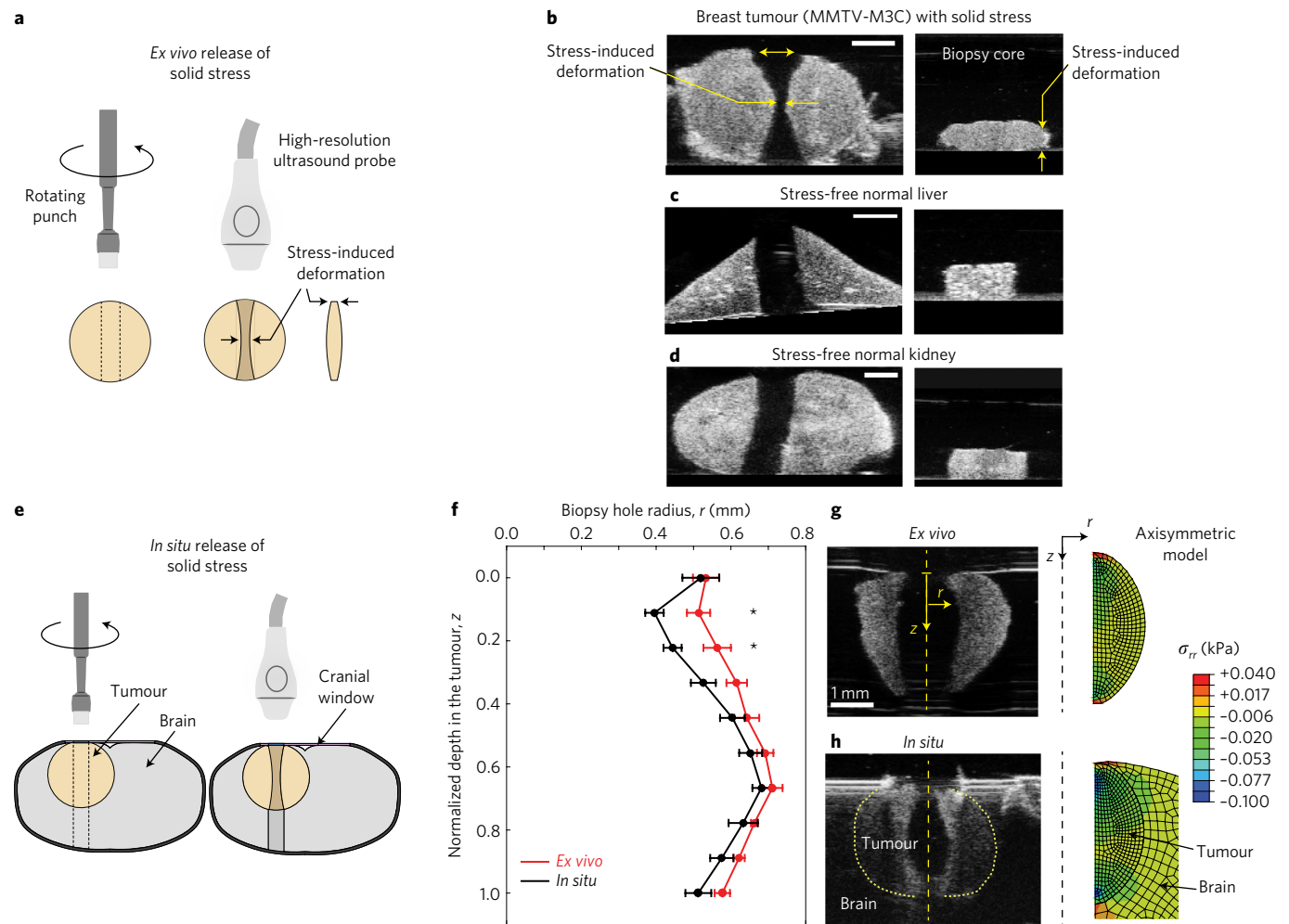


Figure 5 | *In situ* measurements of solid stress. The normal tissue that surrounds the tumour substantially contributes to the state of stress inside the tumour. **a**, The stress was released by punching a cylindrical void in the tumour. The stress relaxation resulted in deformation along the axis of the void: compressive and tensile stresses contracted and enlarged the hole, respectively. The changes in the geometry of the biopsy core are also an indicator of solid stress. **b**, This method is validated on breast tumour (MMTV-M3C), as shown in a representative ultrasound image. **c,d**, In liver (**c**) and kidney (**d**) tissues—control tissues with negligible stored stress—the profile of the biopsy void and core remained constant. Scale bars, 2 mm. **e**, The punching method is capable of *in situ* estimations of solid stress in tissues. The punch can release solid stress in the axis of interest without disturbing the boundary between tumour and surrounding tissue, as schematically shown for the case of brain tumour with an intact normal brain and cranium. **f**, The stress-induced deformation was measured for brain tumour (glioblastoma, U87) *in situ* (by punching the tumour surrounded by brain through a cranial window; $n=5$) and *ex vivo* (by punching surgically excised tumour; $n=4$). $*P<0.05$. **g,h**, Representative ultrasound images of the stress-induced deformation and the respective distribution of radial solid stress, σ_{rr} , the stress at the surface of the punched hole in the r direction, for the *ex vivo* (**g**) and *in situ* (**h**) cases. The solid stress was estimated by an axisymmetric mathematical model that used the stress-induced deformation and the elastic properties of the tumour and the brain as inputs.

of the tumour, consistent with the results obtained by the planar-cut method (Fig. 1d). As expected, the diameter profile of the biopsy void remained unchanged in control tissues (kidney and liver), in which solid stress is negligible (Fig. 5c,d).

In addition to the void left by the biopsied material, the biopsy core also contained useful information about the state of solid stress in the probed tissue. The tip of the core shrank because of the tensile contraction at the periphery, and the diameter in the middle region increased because of the release of compressive stresses (Fig. 5b). The biopsy cores from the control tissues (kidney and liver) did not deform, again because of the negligible solid stress and elastic energy in these tissues (Fig. 5c,d).

Next, we utilized the needle-biopsy method for *in situ* stress measurement and showed that the solid stress in *ex vivo* brain tumours (glioblastoma, U87) is lower in magnitude and different in profile than in tumours that are surrounded by the brain and cranium

(*in situ*; Fig. 5e–g). We used the same glioblastoma model (U87) for which the 2D stress map was quantified in Fig. 1, and released the solid stress via a biopsy punch while the tumour was still surrounded by brain and cranium. For *in situ* measurements, we first made a 2-mm-diameter hole in the cranial window (Fig. 5h) through which we accessed the tumour with a biopsy punch (1.5 mm diameter). The biopsy void reduced in diameter at regions close to the tumour rim, consistent with the 2D map of deformation (Fig. 1d) but in contrast to the primary breast tumours, where the maximum deformation occurred in the centre (Fig. 5b). For *ex vivo* measurements, the tumour was surgically resected from the brain and embedded in 2% agarose; the stress was released by the same biopsy technique (Fig. 5g). We observed an overall smaller deformation for the *ex vivo* tissues than for the *in situ* tissues, and these differences in deformation were notable in regions closer to the outer rim of the tumour (Fig. 5f). Using a mathematical model, the maximum radial

stress for the *in situ* case was estimated as 0.1 kPa in compression compared with 0.02 kPa in the *ex vivo* case.

Discussion

On the basis of the fundamental concept that tissues containing solid stress deform after release from physical confinement, we developed three different experimental techniques and appropriate mathematical models to quantify solid stress and elastic potential energy in solid tumours. The first method, based on releasing solid stress at a plane created by bisecting the tumour, revealed the 2D spatial distribution of solid stress. This method allowed us to distinguish regions with tensile stresses, mostly at the periphery, from the central regions of the tumour that experience mainly compressive stresses. The second method, based on releasing solid stress by creating thin tumour slices, provides a sensitive approach to quantifying low levels of solid stress in small specimens, such as small metastatic lesions in mice. The third method, based on releasing solid stress by core biopsy, is capable of both *in situ* and *ex vivo* estimations of solid stress. The *in situ* feature of this method allowed the determination of the contribution of the surrounding tissue to intratumoral solid stress. Importantly, we found that biopsy cores also undergo *ex vivo* stress-induced deformation and could potentially be used for the measurement of solid stress in the clinic (see Supplementary Table 1 for the capabilities and limitations of each method). These methods overcome the previous technical challenges in measuring these biomechanical abnormalities.

The reliable and precise quantification of solid stress and elastic energy has the potential to promote the discovery of new signalling pathways and therapeutic strategies. The repurposing of losartan¹⁴, an angiotensin receptor inhibitor, and PEGPH20¹⁸, a recombinant hyaluronidase, in cancer therapies is partly based on releasing the mechanical forces exerted on blood vessels in tumours by targeting collagen I and hyaluronic acid. The administration of both drugs increased the efficacy of chemotherapy in preclinical models, leading to two phase II clinical trials^{20,21}. Similar to the earlier method of estimating solid stress⁹, the methods developed here could also be used to compare agents that can lower solid stress. Moreover, characterization of solid stress would help elucidate the relationship between obesity and the cancer immune microenvironment. As we recently found in PDAC tumours^{34,35}, synergies between adipocytes, immune cells and fibroblasts lead to an exacerbated desmoplastic microenvironment during obesity, further promoting blood vessel compression. This is arguably the most important consequence of solid stress demonstrated so far.

Solid stress and elastic energy can also be used as prognostic and diagnostic markers. Factors such as tumour growth pattern and collagen architecture, both closely associated with solid stress, have been shown to have prognostic values. Growth pattern, histologically categorized as pushing versus replacing phenotypes, has been linked to overall survival³⁶ and recurrence risk³⁷. As shown in Fig. 2, colorectal cancer liver metastases with pushing growth patterns have higher elastic energies than pancreatic cancer liver metastases with replacing growth patterns (Supplementary Fig. 7). Furthermore, collagen orientation and alignment have been shown to correlate with prognosis in patients with breast cancer³⁸. As shown, the collagen network in our breast tumour model becomes more organized as the solid stress increases with tumour growth. The quantification of solid stress and its association with growth pattern and collagen architecture suggests that solid stresses may reveal the mechanisms that underlie these histological patterns and lead to further prognostic biomarker discoveries.

The needle-biopsy and planar-cut methods both provide quantitative measurements of solid stress and have potential for use in the clinic. Biopsy samples are obtained routinely during the diagnosis and treatment of cancer; as we show in Fig. 5a,b for the needle-biopsy method, the biopsy core contains useful information about

solid stress in tumours. The solid stress in the biopsy core could be initially evaluated in clinical trials as a new biomarker and used to investigate the mechanism underlying the link between solid stress, collagen orientation and growth patterns. The planar-cut method currently requires the sample to be embedded in agarose and imaged via high-resolution ultrasound; clinically, this procedure may affect the routine processing of tumours by pathologists. To facilitate this procedure, we are working with pathologists to develop methods of generating 3D reconstructions of stress-induced deformation of patient specimens utilizing laser scanning technologies. This methodology will eliminate the agarose-embedding step, shorten the imaging time and provide the strain field in a larger field of view in the tumour and its surrounding tissue; it could be coupled with routine pathological processes on freshly excised tumours. Using fiducial markers, solid stress maps would be matched and compared with histological images from the same cut plane. We expect that clinically accessible and quantitative measurement of solid stress and elastic energy will provide new prognostic and diagnostic markers, similar to those provided by stiffness^{39,40} and interstitial fluid pressure^{41–43}, two mechanical abnormalities that have been used as prognostic biomarkers.

Finally, we used the above methods to demonstrate that elevated solid stress and stiffness are two distinct biomechanical abnormalities. This important distinction implies that attempts to normalize the tumour's mechanical environment should not be limited to decreasing the stiffness. Two of our independent (but consistent) findings demonstrate that (i) primary and metastatic tumours can have substantially different levels of solid stress despite similar stiffness values (Fig. 2e,g) and (ii) solid stress increases with tumour growth, even though stiffness did not change in our tumour models (Fig. 4b,c). These results clearly suggest that the external compressive or tensile solid stresses of tumour cells may be independent of the cellular focal-adhesion forces that are generated in response to changes in the stiffness of the matrix in their vicinity. With the methods and results shown here, we now have the tools to investigate how cancer and stromal cells sense and respond to tensile or compressive forces. And the techniques that we have described will complement our understanding of the effects of altered stiffness⁴⁴.

Methods

Planar-cut method. Releasing solid stress. The 2% agarose was made from low-gelation temperature agarose (Sigma-Aldrich) mixed with PBS buffer. The agarose solution was in a liquid state at 40 °C. The freshly excised tumour was first washed with PBS and then immersed in the liquid agarose inside a custom-made aluminium cast. The cast was then cooled in ice water. After the agarose gel solidified, the tumour–agarose construct was removed from the cast and manually cut with a razor blade at the plane of interest. The solidified agarose that surrounded and held the tumour allowed the tumour to be cut with minimal displacement relative to the gel. One half of the tumour was removed from the gel and fixed in 4% formaldehyde for histological analysis; the other half, still inside the agarose construct, was kept immersed in PBS for at least 10 min to allow the tissue to relax and deform with the release of the solid stress and elastic energy. The same method was used for the control tissues.

Tissue imaging and post-processing. The tissue deformation map was acquired via high-resolution ultrasound (Vevo 2100 system; FUJIFILM Visual Sonics) on the half of the tumour–agarose construct that was immersed and relaxed in PBS. We used the probe MS550S for large samples such as primary breast tumours (depth of view = 13 mm, frequency = 32–56 MHz) and the probe MS700 for smaller samples such as brain tumours (depth of view = 9 mm, frequency = 30–70 MHz). The high-resolution ultrasound provides a resolution of 20–30 µm. For higher resolutions and smaller samples, optical systems such as the OFDI system²⁹ can be used (resolution = 1 µm, depth of view = 2–3 mm). The 3D images were exported from VisualSonics software to MATLAB (The MathWorks) for post-processing. The post-processing included smoothing, which was performed with moving averaging on the top (cut plane) and bottom surfaces of the tumour to remove any noise introduced by ultrasound imaging. The top and bottom surfaces were exported to SolidWorks (Waltham) for 3D reconstruction of the surfaces into a solid object. This solid object was then exported to the compatible finite-element model, as described below.

Mathematical modelling. In the planar-cut method, to translate the stress-induced deformation to solid stress, we developed a mathematical model using the general-purpose commercial finite-element software ABAQUS (Version 6.9, SIMULIA). The 3D geometry of the tumour was imported from the SolidWorks software as described above. We used the element type C3D10, a quadratic tetrahedral element with two elastic parameters: Young's modulus and Poisson's ratio, which were obtained as described below. The assumptions for the use of equation (1) are justified in Supplementary Note 1. We have shown that the viscoelastic time constant is on the order of 10 min (Supplementary Figs 8 and 9) for the length scales comparable to tumour diameter (this time constant is mainly determined by Young's modulus and hydraulic permeability in poroelastic materials^{45,46}). In contrast, the biological processes that give rise to solid stress in tumours, such as proliferation, extracellular-matrix deposition and cell contraction, occur on a timescale that ranges from several hours to several days. Since this is much longer than the viscoelastic time constant, the equilibrium mechanical properties that we are measuring reflect the appropriate properties in the generation and application of solid stress.

The agarose gel was solidified from a liquid state under no external or internal residual stress. Thus, the cut surface in the agarose gel provided the reference plane that represented the original plane of the tumour tissue before stress relaxation in the tumour. A displacement profile was assigned to the top deformed surface of the tumour to translate it back to the original reference plane. This assigned deformation was only in the direction perpendicular to the surface of the tumour (the z direction), and the top surface of the tumour was free to move parallel to the surface direction (the x - y plane). This displacement assignment translates the tumour geometry from the relaxed state (deformed surface) to the original stressed state before the cut (flat surface). The stress component σ_{zz} generated after the displacement assignment is reported as the solid stress in the intact tumour. For *ex vivo* applications of the planar-cut method, the boundary condition on the bottom surface of the tumour was defined as zero force. This assumption is justified for cases such as mouse models of breast tumours where the solid stress field is mainly generated internally and the tumour is not experiencing any major external confinement or resistance. For *in situ* application of the planar-cut method, a contact surface was defined between the tumour and the surrounding normal tissue. In these cases, such as with brain tumours, the normal tissue was also modelled as an elastic material with known Young's modulus, obtained as described below. The solid stress component in the direction perpendicular to the cut surface (z direction) σ_{zz} is reported. The model also reports the elastic energy density, equivalent to the work done to displace the deformation back to the original coordinates, normalized by the tumour volume.

Slicing method. Releasing solid stress. The tumour was embedded in 2% agarose gel as described in the planar-cut method, except that the solidification occurred in a stainless steel cast provided with the commercial VF-300 compressstone (Precisionary Instruments). The tumour-agarose construct, fully immersed in PBS, was then sliced using the compressstone with the desired thickness in the range of 100–500 μm . The tumour slice was detached from the agarose slice, leaving an empty area in the agarose gel. This empty area, here called the 'blank', represents the tumour area before stress relaxation by slicing. The tumour slice was detached from the surrounding agarose manually with a pair of sharp tweezers; detachment occurred spontaneously in some cases. The slice was kept immersed in PBS for at least 10 min while solid stress was released. As a result of stress relaxation, the sample slice underwent expansion in area through different modes of bending and buckling.

Imaging and post-processing. The sample slice and the blank agarose gel were imaged in 3D via high-resolution ultrasound (for larger tumours) or OFDI (for small samples such as a lymph node). The surface areas of both the sample slice and the blank were then calculated by custom in-house MATLAB codes. The change in the ratio of the surface area after stress relaxation to the surface area before stress relaxation (equal to the blank area) was defined as an index of the solid stress and elastic energy.

Needle-biopsy method. Releasing solid stress. The solid stress of the tumour was released by punching a hole with rotating biopsy punches (Integra-Miltex) with diameters of 1.5–3 mm. The rotating punch was made by detaching the stainless steel blade of the biopsy punch from the plastic holder and rotating it with a Dremel rotary tool (Dremel). The rotary punch reduced cutting artefacts by minimizing the mechanical disturbance otherwise caused by non-rotating punching. In *ex vivo* cases, the sample was either held gently by tweezers or embedded in 2% agarose to be secured during the punch. For *in situ* cases such as brain tumours, we made a 2-mm-diameter hole in the plastic coverslip of the cranial window without disturbing the underlying brain tissue. Through this hole in the cranial window, we then punched the brain tumour with a 1.5-mm-diameter punch. The samples were left submerged in PBS for at least 10 min, the time needed for stress relaxation. The biopsy core, which also changed in diameter due to solid stress, was similarly preserved in PBS.

Imaging and post-processing. The stress-induced deformation and the sample geometry were imaged via high-resolution ultrasound as described in the planar-cut method. Using custom in-house semi-automated MATLAB codes we calculated the area of the biopsy hole along the punch axis, from which we calculated the mean hole diameter.

Mathematical modelling. An axisymmetric finite-element code was developed in ABAQUS to translate the stress-induced deformation to the solid stress. A deformation profile was assigned that transformed the deformed punch profile to the original profile before stress relaxation. The original hole profile was simply determined by the biopsy punch diameter, which was uniform along the hole axis (the z axis) and equal to 1.5 mm for small samples such as brain tumours and 2–3 mm for larger samples. In the *ex vivo* cases, a zero-force boundary condition was prescribed at the outer surface of the tumour to simulate the physiological conditions. For *in situ* cases, a contact surface was defined between the tumour and the normal tissue, such as brain, with known elastic properties. We used the four-node axisymmetric element CAX4R for both the tumour and the surrounding tissue. The material properties of both the tumour and the surrounding tissue were obtained via micro and macro measurements of the stiffness, as described below. The stress σ_{rr} , the component of the solid stress on the cut surface, in the direction perpendicular to the axis of the hole (z direction), is reported. The mathematical model also reports the elastic energy density, equivalent to the work done to displace the deformation back to the original coordinates, normalized by the volume of the tumour.

Micro and macro measurement of tumour stiffness. The stiffness of the tumours was measured using AFM on the microscale as the indentation modulus, and on the macroscale as the unconfined compression modulus. For both cases, the measurement was obtained within 1 h after excision of the tumours. The samples were maintained in PBS with protease inhibitors (Complete Protease cocktail tablets, Roche Applied Science) at 4 °C before testing. All of the measurements were performed in near-physiological PBS at ambient temperature (25 °C).

AFM-based measurement of the indentation modulus. The indentation moduli of tumours were quantified using an Asylum MFP3D AFM (Asylum). We used polystyrene colloidal probe tips with an end radius (R) of $\sim 12.5 \mu\text{m}$ (Polysciences) attached to tipless cantilevers with nominal spring constant $k \sim 0.12 \text{ N m}^{-1}$ (Bruker). The colloidal probes were attached to the cantilever by the lift-off process: a dot of glue (M-Bond 610, Structure Probes/SPI Supplies) was placed on a tipless cantilever by making quick contact between the cantilever and a thin layer of glue (1 μl thick) spread over a 10 mm \times 10 mm mica surface. We then made immediate contact between the tip of the cantilever and a colloid probe resting on a glass slide and waited for 1 min with the cantilever pushing against the colloid. This process was followed by heat curing for 2 h at 150 °C. For each probe tip, the exact spring constants of the cantilevers were directly measured using the thermal calibration method⁴⁷. The relationship between the detected voltage and the applied force was calibrated by bringing the cantilever into contact with a glass slide and calculating the slope of the voltage–displacement curve. The displacement, d , was translated to force, F , using Hooke's law ($F = kd$). The indentation was performed under a force control scheme (maximum force $\sim 20 \text{ nN}$) limiting the indentation depths to 0.5–3 μm . The tip displacement was obtained by subtracting the cantilever deflection from the vertical movement of the piezoelectric actuator. An indentation approach velocity of 2 $\mu\text{m s}^{-1}$ ensured that the elastic modulus was probed at a lower rate, close to equilibrium conditions.

The effective indentation modulus E_{ind} was computed using Hertzian contact mechanics models via least-squares linear regression of the experimental loading force–displacement curves. For the spherical colloidal probe tip with end radius R on the sample with thickness $h \gg R$ (here, $h \sim 5 \text{ mm}$, $R \sim 12.5 \mu\text{m}$)

$$F = \frac{4}{3} \frac{E_{\text{ind}}}{(1 - \nu^2)} R^{1/2} D^{3/2}$$

where F is the indentation force and D is the indentation depth (we assumed $\nu = 0.1$, as measured in other soft tissues^{48,49}). A representative force–displacement curve is shown in Supplementary Fig. 10.

Macroscale unconfined compression test. Young's moduli of tumours were determined by unconfined compression tests⁵⁰. Slices of freshly excised tissue, 3 mm in diameter and $\sim 2 \text{ mm}$ thick, were placed in an unconfined compression chamber submerged in PBS. The chamber was mounted in an ultrasensitive servo-controlled materials tester (Dynastat Mechanical Spectrometer; IMASS). Each specimen was compressed by 5% of the original height in ramps of 20 s and allowed to relax for 20 min. Four successive measurements were performed with each tissue slice. Young's modulus was determined as the ratio of the linear fit to stress–strain data (Supplementary Fig. 8).

Cell culture. Cells (MMTV-M3C, AK4.4, SL4, U87, 4T1) were cultured in DMEM (ATCC 30-2002) medium containing 10% fetal bovine serum. Cells were harvested at $\sim 80\%$ confluency, washed twice with PBS, counted and re-suspended in DMEM before injection. All cell lines repeatedly tested

negative for mycoplasma using the Mycoalert Plus Mycoplasma Detection Kit (Lonza), authenticated before use by IDEXX laboratories.

Tumour models. *Primary tumour models.* MMTV-M3C cells (*Her2+*) were provided by P. Huang (Massachusetts General Hospital, Boston, Massachusetts, USA) and were isolated from lung metastases of mammary adenocarcinomas in mice generating spontaneous mammary tumours (MMTV-PyVT). Orthotopic breast tumours were generated by implanting a small piece (1 mm³) of viable tumour tissue (from a source tumour in a separate animal) or by injection of 1×10^5 cells into the mammary fat pad of a 6- to 8-week-old female FVB mouse (MMTV-M3C). AK4.4 cells (*Kras*^{G12D} and *p53*^{+/-}) were provided by N. Bardeesy (Massachusetts General Hospital, Boston, Massachusetts, USA) and were isolated from mice generating spontaneous pancreatic tumours (*Ptfl1-Cre/LSL-Kras*^{G12D}/*p53*^{lox/+}). Orthotopic pancreatic tumours were similarly generated by implanting a small piece (1 mm³) of viable tumour tissue into the pancreas of a 6- to 8-week-old male FVB mouse (AK4.4 model). The SL4 mouse colorectal cancer cells were provided by T. Irimura⁵¹. For the orthotopic SL4 model, 5×10^5 cells in 10 μ l of PBS and extracellular-matrix-rich gel (Corning Matrigel) were injected into the caecal wall between the serosa and mucosa from the serosa side using an insulin syringe with a 27G needle. For the glioblastoma model, cranial windows were implanted into nude mice as previously described⁵², and the mice were allowed to recover for 1 week before tumour implantation. U87 fragments (0.2–0.3 mm in diameter; from a source tumour in a separate animal) were implanted into the left cerebral hemisphere 0.5–1 mm deep in 6- to 8-week-old female nude mice. All animal procedures were carried out following the Public Health Service Policy on Humane Care of Laboratory Animals and were approved by the Institutional Animal Care and Use Committee of Massachusetts General Hospital.

Liver metastasis model. Mice were anaesthetized with an intraperitoneal injection of ketamine (100 mg per kg) and xylazine (10 mg per kg). A left-flank incision was made through the skin and abdominal wall, and the spleen was exteriorized. The middle of the spleen was ligated with a suture before transection, with the goal of preserving the vascular pedicles to both hemispleens. 1×10^5 cells (AK4.4 or SL4) in 100 μ l DMEM were injected slowly into the distal lobe with a 30G needle. After 10 min, the hemispleen used for tumour cell injection was resected. The remaining spleen was placed back into the abdomen. The abdominal wall was closed with a continuous suture. The skin was closed with surgical staples.

Lymph node spontaneous metastasis. 2×10^5 4T1 cells in DMEM were injected into the second mammary fat pad of syngeneic BALB/c mice. On day 15 post-injection, the primary tumour was resected. Animals were killed 2–3 weeks post-resection to evaluate the metastatic lymph nodes.

Histology. Before death, mice were slowly (~2 min) injected with 100 μ l of 1 mg per ml fluorescein isothiocyanate (FITC)-conjugated lectin (Vector Labs) via the tail vein 5 min before tumour removal, long enough for FITC-lectin to reach perfused vessels. The tumours were then excised, fixed in 4% formaldehyde in PBS overnight and embedded in paraffin blocks. Transverse tumour sections, 5 μ m thick, were immunostained with antibodies for endothelial marker CD31 (DIA310, Dianova, 1:100 dilution) and counterstained with DAPI (Vector Labs). Collagen I and hyaluronan were, respectively, detected using the LF-68 antibody (1:500 dilution) provided by Larry Fisher (NIDCR) and a biotinylated hyaluronan proteoglycan fragment (385911, Calbiochem). For the detection of collagen I, the paraffin-embedded sections were treated with a pH-9.0 trypsin antigen-retrieval solution and counterstained with DAPI. Staining for α SMA (C6198 antibody, Sigma, 1:100 dilution) was also carried out. The entire tumour section at $\times 10$ magnification was taken from each slide using a confocal microscope (Olympus) or slide scanner (TissueFAXS). For vascular analysis, vessels were segmented using a custom semi-automated tracing program developed in MATLAB, allowing the analysis of each vessel according to its size and staining intensity. Tumour perfusion was assessed by identifying the fraction of CD31+ vessels that were also positive for FITC-lectin, indicating that those individual vessels were perfused before the mice were killed, and are therefore functional and uncompressed.

Collagenase treatment. The collagenase (Sigma-Aldrich) solution was prepared by dissolving 10 mg collagenase in 10 ml DMEM. After excision, the tumour was placed in the collagenase solution remaining at 37 °C for 2 h before solid stress measurement.

Statistical analysis. The data are presented as the mean \pm standard error of the mean. Groups were compared using an unpaired two-sided Student's *t*-test (due to independent sampling) with equal or unequal variance. The variance similarity was tested via *F*-test with *P* = 0.05. All of the results are based on pilot studies (not reported) preceding the main experiments (reported). The sample size for the main experiments were determined from the pilot studies. Mice were size-matched as appropriate for each experiment. No additional blinding or randomization was required for the animal studies.

Code availability. Custom scripts for MATLAB are available in the Supplementary Information.

Data availability. Source data for the figures in this study are available in figshare with the identifier <https://dx.doi.org/10.6084/m9.figshare.3796092> (ref. 53). The authors declare that all other data supporting the findings of this study are available within the paper and its Supplementary Information.

Received 21 April 2016; accepted 11 August 2016;
published 28 November 2016

References

- Jain, R. K., Martin, J. D. & Stylianopoulos, T. The role of mechanical forces in tumor growth and therapy. *Annu. Rev. Biomed. Eng.* **16**, 321–346 (2014).
- Chaudhuri, O. *et al.* Extracellular matrix stiffness and composition jointly regulate the induction of malignant phenotypes in mammary epithelium. *Nat. Mater.* **13**, 970–978 (2014).
- Mouw, J. K. *et al.* Tissue mechanics modulate microRNA-dependent PTEN expression to regulate malignant progression. *Nat. Med.* **20**, 360–367 (2014).
- Samuel, M. S. *et al.* Actomyosin-mediated cellular tension drives increased tissue stiffness and β -catenin activation to induce epidermal hyperplasia and tumor growth. *Cancer Cell* **19**, 776–791 (2011).
- Wirtz, D., Konstantopoulos, K. & Searson, P. C. The physics of cancer: the role of physical interactions and mechanical forces in metastasis. *Nat. Rev. Cancer* **11**, 512–522 (2011).
- Goetz, J. G. *et al.* Biomechanical remodeling of the microenvironment by stromal caveolin-1 favors tumor invasion and metastasis. *Cell* **146**, 148–163 (2011).
- Tung, J. C. *et al.* Tumor mechanics and metabolic dysfunction. *Free Radic. Biol. Med.* **79**, 269–280 (2015).
- Helmlinger, G., Netti, P. A., Lichtenbeld, H. C., Melder, R. J. & Jain, R. K. Solid stress inhibits the growth of multicellular tumor spheroids. *Nat. Biotechnol.* **15**, 778–783 (1997).
- Stylianopoulos, T. *et al.* Causes, consequences, and remedies for growth-induced solid stress in murine and human tumors. *Proc. Natl Acad. Sci. USA* **109**, 15101–15108 (2012).
- Boucher, Y. & Jain, R. K. Microvascular pressure is the principal driving force for interstitial hypertension in solid tumors: implications for vascular collapse. *Cancer Res.* **52**, 5110–5114 (1992).
- Griffon-Etienne, G., Boucher, Y., Brekken, C., Suit, H. D. & Jain, R. K. Taxane-induced apoptosis decompresses blood vessels and lowers interstitial fluid pressure in solid tumors: clinical implications. *Cancer Res.* **59**, 3776–3782 (1999).
- Padera, T. P. *et al.* Lymphatic metastasis in the absence of functional intratumor lymphatics. *Science* **296**, 1883–1886 (2002).
- Padera, T. P. *et al.* Pathology: cancer cells compress intratumour vessels. *Nature* **427**, 695 (2004).
- Chauhan, V. P. *et al.* Angiotensin inhibition enhances drug delivery and potentiates chemotherapy by decompressing tumour blood vessels. *Nat. Commun.* **4**, 2516 (2013).
- Jain, R. K. Antiangiogenesis strategies revisited: from starving tumors to alleviating hypoxia. *Cancer Cell* **26**, 605–622 (2014).
- Fernández-Sánchez, M. E. *et al.* Mechanical induction of the tumorigenic β -catenin pathway by tumour growth pressure. *Nature* **523**, 92–95 (2015).
- Tse, J. M. *et al.* Mechanical compression drives cancer cells toward invasive phenotype. *Proc. Natl Acad. Sci. USA* **109**, 911–916 (2012).
- Provenzano, P. P. *et al.* Enzymatic targeting of the stroma ablates physical barriers to treatment of pancreatic ductal adenocarcinoma. *Cancer Cell* **21**, 418–429 (2012).
- Chauhan, V. P. *et al.* Compression of pancreatic tumor blood vessels by hyaluronan is caused by solid stress and not interstitial fluid pressure. *Cancer Cell* **26**, 14–15 (2014).
- US National Library of Medicine. Proton w/FOLFIRINOX-Losartan for pancreatic cancer. *ClinicalTrials.gov* <https://clinicaltrials.gov/ct2/show/NCT01821729> (2013).
- US National Library of Medicine. PEGPH20 plus nab-paclitaxel plus Gemcitabine compared with nab-paclitaxel plus Gemcitabine in subjects with stage IV untreated pancreatic cancer (HALO-109-202). *ClinicalTrials.gov* <https://clinicaltrials.gov/ct2/show/NCT01839487> (2013).
- Chuong, C. & Fung, Y. in *Frontiers in Biomechanics* (eds Schmid-Schönbein, G. W. *et al.*) Ch. 9 (Springer, 1986).
- Taber, L. A. & Humphrey, J. D. Stress-modulated growth, residual stress, and vascular heterogeneity. *J. Biomech. Eng.* **123**, 528–535 (2001).
- Campas, O. *et al.* Quantifying cell-generated mechanical forces within living embryonic tissues. *Nat. Methods* **11**, 183–189 (2014).
- Grashoff, C. *et al.* Measuring mechanical tension across vinculin reveals regulation of focal adhesion dynamics. *Nature* **466**, 263–266 (2010).

26. Timoshenko, S. & Goodier, J. N. *Theory of Elasticity* (McGraw-Hill, 1951).
27. Plodinec, M. *et al.* The nanomechanical signature of breast cancer. *Nat. Nanotech.* **7**, 757–765 (2012).
28. Lopez, J., Kang, I., You, W., McDonald, D. & Weaver, V. *In situ* force mapping of mammary gland transformation. *Integr. Biol. (Camb)*, **3**, 910–921 (2011).
29. Vakoc, B. J. *et al.* Three-dimensional microscopy of the tumor microenvironment *in vivo* using optical frequency domain imaging. *Nat. Med.* **15**, 1219–1223 (2009).
30. Simon, D., Horgan, C. & Humphrey, J. Mechanical restrictions on biological responses by adherent cells within collagen gels. *J. Mech. Behav. Biomed. Mat.* **14**, 216–226 (2012).
31. Orimo, A. *et al.* Stromal fibroblasts present in invasive human breast carcinomas promote tumor growth and angiogenesis through elevated SDF-1/CXCL12 secretion. *Cell* **121**, 335–348 (2005).
32. Stylianopoulos, T. *et al.* Coevolution of solid stress and interstitial fluid pressure in tumors during progression: implications for vascular collapse. *Cancer Res.* **73**, 3833–3841 (2013).
33. Voutouri, C., Mpekris, F., Papageorgis, P., Odysseos, A. D. & Stylianopoulos, T. Role of constitutive behavior and tumor-host mechanical interactions in the state of stress and growth of solid tumors. *PLoS ONE* **9**, e104717 (2014).
34. Fukumura, D., Incio, J., Shankaraiah, R. & Jain, R. K. Obesity and cancer: an angiogenic and inflammatory link. *Microcirculation* **23**, 191–206 (2016).
35. Incio, J. *et al.* Obesity-induced inflammation and desmoplasia promote pancreatic cancer progression and resistance to chemotherapy. *Cancer Discov.* **6**, 852–869 (2016).
36. Van den Eynden, G. G. *et al.* The histological growth pattern of colorectal cancer liver metastases has prognostic value. *Clin. Exp. Metastasis* **29**, 541–549 (2012).
37. Eefsen, R. *et al.* Growth pattern of colorectal liver metastasis as a marker of recurrence risk. *Clin. Exp. Metastasis* **32**, 369–381 (2015).
38. Conklin, M. W. *et al.* Aligned collagen is a prognostic signature for survival in human breast carcinoma. *Am. J. Pathol.* **178**, 1221–1232 (2011).
39. Good, D. W. *et al.* Elasticity as a biomarker for prostate cancer: a systematic review. *BJU. Int.* **113**, 523–534 (2014).
40. Choi, W. J. *et al.* Predicting prognostic factors of breast cancer using shear wave elastography. *Ultrasound Med. Biol.* **40**, 269–274 (2014).
41. Milosevic, M. F. *et al.* High tumor interstitial fluid pressure identifies cervical cancer patients with improved survival from radiotherapy plus cisplatin versus radiotherapy alone. *Int. J. Cancer* **135**, 1692–1699 (2014).
42. Roh, H. *et al.* Interstitial hypertension in carcinoma of uterine cervix in patients: possible correlation with tumor oxygenation and radiation response. *Cancer Res.* **51**, 6695–6698 (1991).
43. Fyles, A. *et al.* Long-term performance of interstitial fluid pressure and hypoxia as prognostic factors in cervix cancer. *Radiother. Oncol.* **80**, 132–137 (2006).
44. Discher, D. E., Janmey, P. & Wang, Y. L. Tissue cells feel and respond to the stiffness of their substrate. *Science* **310**, 1139–1143 (2005).
45. Nia, H. T., Han, L., Li, Y., Ortiz, C. & Grodzinsky, A. Poroelasticity of cartilage at the nanoscale. *Biophys. J.* **101**, 2304–2313 (2011).
46. Grodzinsky, A. J. *Fields, Forces, and Flows in Biological Systems* Ch. 4 (Garland Science, 2011).
47. Hutter, J. L. & Bechhoefer, J. Calibration of atomic-force microscope tips. *Rev. Sci. Instrum.* **64**, 1868–1873 (1993).
48. Kiviranta, P. *et al.* Collagen network primarily controls Poisson's ratio of bovine articular cartilage in compression. *J. Orthop. Res.* **24**, 690–699 (2006).
49. Buschmann, M. D. *et al.* Stimulation of aggrecan synthesis in cartilage explants by cyclic loading is localized to regions of high interstitial fluid flow. *Arch. Biochem. Biophys.* **366**, 1–7 (1999).
50. Netti, P. A., Berk, D. A., Swartz, M. A., Grodzinsky, A. J. & Jain, R. K. Role of extracellular matrix assembly in interstitial transport in solid tumors. *Cancer Res.* **60**, 2497–2503 (2000).
51. Morimoto-Tomita, M., Ohashi, Y., Matsubara, A., Tsuiji, M. & Irimura, T. Mouse colon carcinoma cells established for high incidence of experimental hepatic metastasis exhibit accelerated and anchorage-independent growth. *Clin. Exp. Metastasis* **22**, 513–521 (2005).
52. Yuan, F. *et al.* Vascular permeability and microcirculation of gliomas and mammary carcinomas transplanted in rat and mouse cranial windows. *Cancer Res.* **54**, 4564–4568 (1994).
53. Nia, H. T. *et al.* Dataset for solid stress and elastic energy as measures of tumour mechanopathology. *figshare* <http://dx.doi.org/10.6084/m9.figshare.3796092> (2016).

Acknowledgements

We thank S. Roberge, C. Smith, J. Kahn and M. Duquette for technical assistance. We also thank P. Huang, N. Bardeesy and T. Irimura for providing MMTV-M3C, AK4.4 and SL4 cells, respectively. This work was supported in part by funding from the National Cancer Institute (P01-CA080124), an NCI Outstanding Investigator Award (R35-CA197743) and a Department of Defense Breast Cancer Research Innovator award (W81XWH-10-1-0016) to R.K.J., a DP2 OD008780 to T.P.P., a R01 grant (HL128168) to L.L.M., T.P.P. and J.W.B., a Susan G. Komen Foundation Fellowship (PDF14301739) to G.S., a National Institutes of Health award (F31HL126449) to M.D., and an UNCF-Merck Science Initiative Postdoctoral Fellowship, Burroughs Wellcome Fund Postdoctoral Enrichment Program Award and a NCI grant (F32CA183465) to D.J.

Author contributions

H.T.N. and R.K.J. designed the study; H.T.N., H.L., G.S., M.D., D.J., N.R., J.I., K.J. performed the research; H.T.N., H.L., G.S., M.D., D.J., N.R., J.I., V.P.C., K.J., J.D.M., V.A., T.P.P., D.F., Y.B., F.J.H., A.J.G., J.W.B., L.L.M. and R.K.J. analysed the data; H.T.N., M.D., G.S., V.P.C., L.L.M. and R.K.J. wrote the manuscript.

Additional information

Supplementary information is available for this paper.

Reprints and permissions information is available at www.nature.com/reprints.

Correspondence and requests for materials should be addressed to R.K.J.

How to cite this article: Nia, H. T. *et al.* Solid stress and elastic energy as measures of tumour mechanopathology. *Nat. Biomed. Eng.* **1**, 0004 (2016).

Competing interests

R.K.J. received consultant fees from Ophthotech, SPARC, SynDevRx and XTuit. R.K.J. owns equity in Enlight, Ophthotech, SynDevRx and XTuit, and serves on the Board of Directors of XTuit and the Boards of Trustees of Tekla Healthcare Investors, Tekla Life Sciences Investors, the Tekla Healthcare Opportunities Fund and the Tekla World Healthcare Fund. No reagents or funding from these companies were used in these studies.